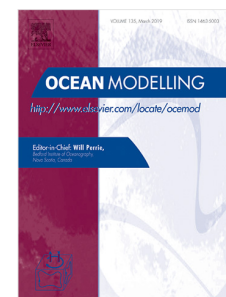


Journal Pre-proof

Parameter estimation for a global tide and surge model with a memory-efficient order reduction approach

Xiaohui Wang, Martin Verlaan, Maialen Irazoqui Apecechea, Hai Xiang Lin



PII: S1463-5003(22)00051-8

DOI: <https://doi.org/10.1016/j.ocemod.2022.102011>

Reference: OCEMOD 102011

To appear in: *Ocean Modelling*

Received date: 10 June 2021

Revised date: 17 March 2022

Accepted date: 19 April 2022

Please cite this article as: X. Wang, M. Verlaan, M.I. Apecechea et al., Parameter estimation for a global tide and surge model with a memory-efficient order reduction approach. *Ocean Modelling* (2022), doi: <https://doi.org/10.1016/j.ocemod.2022.102011>.

This is a PDF file of an article that has undergone enhancements after acceptance, such as the addition of a cover page and metadata, and formatting for readability, but it is not yet the definitive version of record. This version will undergo additional copyediting, typesetting and review before it is published in its final form, but we are providing this version to give early visibility of the article. Please note that, during the production process, errors may be discovered which could affect the content, and all legal disclaimers that apply to the journal pertain.

© 2022 The Author(s). Published by Elsevier Ltd. This is an open access article under the CC BY license (<http://creativecommons.org/licenses/by/4.0/>).

Parameter Estimation for a Global Tide and Surge Model with a Memory-Efficient Order Reduction Approach

Xiaohui Wang^{a,*}, Martin Verlaan^{a,b}, Maialen Irazoqui Apecechea^b, Hai Xiang Lin^a

^a*Delft Institute of Applied Mathematics, Delft University of Technology, Mekelweg 4, 2628 CD, Delft, The Netherlands*

^b*Deltas, P.O.Box 177, Delft, 2600 MH, The Netherlands*

Abstract

Accurate parameter estimation for the Global Tide and Surge Model (GTSM) benefits from observations with long time-series. However, increasing the number of measurements leads to a large computation demand and increased memory requirements, especially for the ensemble-based methods that assimilate the measurements at one batch. In this study, a memory-efficient parameter estimation scheme using model order reduction in time patterns is developed for a high-resolution global tide model. We propose using projection onto empirical time-patterns to reduce the model output time-series to a much smaller linear subspace. Then, to further improve the estimation accuracy, we introduce an outer-loop, similar to Incremental 4D-VAR, to evaluate model-increments at a lower resolution and subsequently reduce the computational cost. The inner-loop optimizes parameters using the lower-resolution model and an iterative least-squares estimation algorithm called DUD. The outer-loop updates the initial output from the high-resolution model with updated parameters from the converged inner-loop and then restarts the inner-loop. We performed experiments to adjust the bathymetry with observations from the FES2014 dataset. Results show that the time patterns of the tide series can be successfully projected to a lower dimen-

*Corresponding author

Email addresses: X.Wang-13@tudelft.nl (Xiaohui Wang),
 Martin.Verlaan@deltas.nl (Martin Verlaan), Maialen.Irazoqui@deltas.nl
 (Maialen Irazoqui Apecechea), H.X.Lin@tudelft.nl (Hai Xiang Lin)

sional subspace, and memory requirements are reduced by a factor of 22 for our experiments. The estimation is converged after three outer iterations in our experiment, and tide representation is significantly improved, achieving a 34.5% reduction of error. The model's improvement is not only shown for the calibration dataset, but also for several validation datasets consisting of one year of time-series from FES2014 and UHSLC tide gauges.

Keywords: Global tide and surge model, Parameter estimation, Model order reduction

1. Introduction

The risk from coastal flooding generally increases due to the sea level rise and climate changes (Jongman et al., 2012; Muis et al., 2017). The sea level can reach especially high values where tidal amplitudes are large. It is even more destructive, especially when the storm surge coincides with the high-water during spring tide (Pugh, 1996). Hydrodynamic tide and storm-surge models play an important role in assessments of flood risk and sea level rise and for forecasting. Extreme sea levels are often a combination of high tides and a storm surge. The accuracy of the reproduction of both tides and storm surge is important for these applications (Ward et al., 2015). In deep water, tides and storm surge can be modelled independently, but in shallow water non-linear interactions are more prominent. With the future aim to model these interactions, we develop a combined global tide and surge model (GTSM). However, this paper focuses on the tides and considers tides separately. Stammer et al. (2014) summarized the developments in global tide modelling and compared a number of global tide models regarding their physical processes, grid resolution and so on. There are still a number of sources of model errors remaining, such as neglected physics in the model formulation, uncertainty parameters (e.g., bathymetry), bottom friction, and internal tides friction that are not accurately known. Data assimilation is a promising approach for reducing parameter uncertainties with available observation data, e.g., altimeter and tide gauge measurements. Several successful applications of data assimilation for improving tide model performance have been reported in literatures (Edwards et al., 2015) with the adjoint method (Das and Lardner, 1991; Bannister, 2017; Heemink et al., 2002; Zaron, 2019), and ensemble methods (Barth et al., 2010; Mayo et al., 2014; Ngodock et al., 2016; Zijl et al., 2013). In a comparison of several assimilative and non-assimilative

28 models, Stammer et al. (2014) reports that data assimilation can contribute
29 significantly to the accuracy of global tide models.

30 In our previous study, we proposed a computation-efficient parameter es-
31 timation scheme to estimate bathymetry for a high-resolution Global Tide
32 and Surge Model (GTSM) (Wang et al., 2021). GTSM is a 2D tide and
33 surge model with an unstructured grid. The model is running operationally
34 to forecast storm surges worldwide. Another application of GTSM is the as-
35 sessment of flood risks and the potential impacts of sea level rise to extreme
36 storm tides (Verlaan et al., 2015). In Wang et al. (2021), after the parame-
37 ter estimation tide representation in GTSM was improved significantly using
38 an ensemble type algorithm without the adjoint called DUD (Ralston and
39 Jennrich, 1978). DUD (Does not use derivative) is a derivative-free calibra-
40 tion algorithm that works in an iterative way. In the estimation procedure,
41 observation is compared with the model output in the time series formula.
42 Tidal constituents are widely used as model output in estimation applica-
43 tions, such as the estimation of the FES model (Lyard et al., 2021). But
44 tidal constituents cannot be directly computed in GTSM because GTSM is
45 a time-stepping model. The Time-stepping model allows a more accurate
46 representation of non-linear interactions at the coast, which is also recog-
47 nized by Lyard et al. (2021). To obtain accurate tidal analysis results, we
48 have to simulate the GTSM for a year based on the Rayleigh criterion to
49 separate diurnal constituent S1 from K1. If one would include seasonal con-
50 stituents Sa and Ssa, several years would be required since they show large
51 inter-annual variability. Harmonic analysis needs a careful consideration of
52 which tidal constituents to be included. When the length of the time-series is
53 not an integer multiple of the period given by the frequency difference of two
54 constituents, or a large non-integer value, then the estimation is potentially
55 poorly conditioned, and the estimates will influence each other. In contrast,
56 the proposed time-series POD method will produce accurate orthogonal ap-
57 proximations without any user intervention and regardless of the length of
58 the time-series. In addition, hundreds of model runs would be simulated in
59 the estimation process. Therefore, parameter estimation in tidal constituents
60 is not feasible with the computational facilities available to us. The use of
61 time series for weeks or a month can significantly reduce the simulation time
62 and computational complexity. But the simulation time length of two weeks
63 (one spring-neap cycle) is short and leads to estimates that over-fit the data
64 to some extent (Wang et al., 2021). However, longer time series imply larger
65 memory requirements in the analysis step, which is not feasible for the current

66 implementation and computational cluster. Therefore, an efficient approach
 67 has to be designed which can reduce the memory requirement and enable a
 68 longer simulation time length.

69 For ensemble-based data assimilation methods (Evensen, 1994), the mem-
 70 ory use is proportional to the number of measurements assimilated in one
 71 batch multiplied by the number of perturbed model runs, called ensemble
 72 members. This also applies to the method used in this paper. Observations
 73 are often assimilated in one batch to maintain consistency between the esti-
 74 mated parameters and model output after the estimation (Evensen and van
 75 Leeuwen, 2000; Emerick and Reynolds, 2013), which cannot be guaranteed
 76 for incremental assimilation in smaller batches. However, this leads to a
 77 large size of the linearized model outputs $O(NN_tN_s)$, where N, N_t, N_s are
 78 the number of ensembles, number of observation time steps, and number of
 79 locations, respectively. When we attempt to include more observations and
 80 to estimate more parameters, this can result in a huge memory usage on a
 81 single compute-node. There are at least two ways to ease the huge memory us-
 82 age problem: 1. parallelization of the linear solver; and 2. reducing the size
 83 of the problem by approximation. Here we follow the second approach by
 84 using model order reduction methods. Note that variational methods have
 85 different characteristics in terms of memory usage.

86 Model Order Reduction (MOR) is a collection of methods that can be
 87 used to reduce the computational complexity of mathematical models in nu-
 88 matical simulations with an approximation of the original model (Antoulas
 89 et al., 2015). In this paper, we develop a new method time-POD, which aims
 90 to reduce the size of the model output, so that the memory needed for data
 91 assimilation can be reduced. The method was inspired by the Proper Orthog-
 92 onal Decomposition (POD) (Chatterjee, 2000), which projects the spatial
 93 patterns of the state onto the leading singular vectors. Here we project onto
 94 the leading singular vectors of the time patterns instead. POD is one of the
 95 MOR techniques first introduced in fluid dynamics by Lumley (1967). It was
 96 already known as the Karhunen-Loëve expansion (Kosambi, 1943) in statis-
 97 tics, and also as Principal Component Analysis (PCA) (Jolliffe and Cadima,
 98 2016) or Empirical Orthogonal Functions (EOF) (Monahan et al., 2009) in
 99 meteorology. POD methods (Liang et al., 2002), such as the Karhunen-Loëve
 100 decomposition (KLD), PCA, and Singular Value Decomposition (SVD), have
 101 been applied in various fields such as fluid dynamics (Cazemier et al., 1998),
 102 pattern recognition (Kopp et al., 1997), and more recently in control theory
 103 and inverse problems.

104 MOR has been applied in both ensemble-based and variational data as-
 105 similation systems (Cane et al., 1996; Farrell and Ioannou, 2001; Beck and
 106 Ehrendorfer, 2005; Cao et al., 2007). The typical application of MOR is pro-
 107 jected based on truncated characteristic vectors in spatial patterns of model
 108 state variables. For instance, a dual-weighted proper orthogonal decompo-
 109 sition (DWPOD) is proposed combining with four-dimensional variational
 110 method (4DVar) to reduce state space orders in a global shallow-water model
 111 (Daescu and Navon, 2008). Lin and McLaughlin (2014) reduced the param-
 112 eter dimension by POD for an EnKF data assimilation system.

113 In this study, we proposed two new developments based on our previous
 114 estimation scheme (Wang et al., 2021) . Firstly, a low memory storage estima-
 115 tion approach is implemented using the model order reduction techniques in
 116 the time patterns. Secondly, the implementation of outer-iteration improves
 117 the estimation accuracy, the reason is to better deal with the optimization of
 118 non-linear models. Dud is an iterative smoother type estimation algorithm,
 119 the memory needed is linearly increased with the simulation time length. The
 120 total data size is in the order of $O(10^9)$ when the time length is larger than
 121 one month in this application, which leads to memory issues. Therefore, we
 122 developed a time-POD approach to reduce the dimension of the model out-
 123 put by project the time space of the model output onto a smaller subspace.
 124 The main advantage of the time-POD is that the simulation required is not
 125 restricted by the Rayleigh criterion, which normally requires a year's simu-
 126 lation for accurate estimation of tidal constituents. The projection reduces
 127 the memory requirements while still accurately representing the time signal
 128 for any simulation length. The required length of the time-span considered
 129 then becomes limited by other considerations. In our previous experiments,
 130 a length of two weeks leads to some over-fitting for that time period (Wang
 131 et al., 2021). In this study, we performed the time-POD calibration experi-
 132 ments covering the one-month simulation time span. It provides significant
 133 improvements to the model accuracy and reduce the over-fitting of data used
 134 in the estimation process.

135 Furthermore, parameter estimation accuracy is also affected by the cal-
 136 ibration algorithm. The approach of using a lower resolution model in the
 137 estimation is similar to Incremental 4Dvar, and an outer loop iteration can
 138 further improve the estimation accuracy by updating the reference using a
 139 new fine resolution simulation with the updated parameters (Emerick and
 140 Reynolds, 2013; Chen and Oliver, 2013). The incremental 4D-Var method
 141 consists of nested inner-loops and outer-loops to reduce computational cost

for data assimilation. It is applied successfully in the assimilation system at the ECMWF (Courtier et al., 1994; Mahfouf and Rabier, 2000; Trémolet, 2007). In this study, we use a very similar structure. Coarse Incremental Estimation (Wang et al., 2021) uses a coarser grid to represent the model increments between the initial model and model with updated parameters. The outer loop uses the high-resolution model with the updated parameters from the converged inner-loop to restart the estimation process. It is expected that this will result in a better match between the observations and the fine grid model.

In Section 2, the Global Tide and Surge Model (GTSM) is introduced. Section 3 describes the parameter estimation scheme, including the time-POD application to temporal patterns and the outer loop implementation. Section 4 describes the experiment configuration including parameter selection, observations, model and experiments set-up. In Section 5, POD performance is evaluated by firstly analyzing the accuracy of projected and reconstructed model output and secondly, comparing the bathymetry estimation results with or without the application of MOR. We also perform a parameter estimation experiment with an extended simulation time of one month. Model validation for the year 2014 is presented in Section 6. Finally, discussions and conclusions follow in Section 7.

2. Global Tide and Surge Model

GTSM is a depth-averaged hydrodynamic model that simulates tide and surges. It plays an important role in the Global Storm Surge Information System (GLOSSIS) to provide water level and storm surge forecasts. The model is forced by tide generating forces without any lateral boundaries. The governing equations of the model are:

$$\begin{aligned} \frac{\partial \mathbf{u}}{\partial t} + \frac{1}{h}(\nabla \cdot (h\mathbf{u}\mathbf{u}) - \mathbf{u}\nabla \cdot (h\mathbf{u})) + \mathbf{f} \times \mathbf{u} \\ = -g\nabla(\zeta - \zeta_{EQ} - \zeta_{SAL}) + \nabla \cdot (\nu(\nabla \mathbf{u} + \nabla \mathbf{u}^T)) + \frac{\tau}{h} \\ \frac{\partial h}{\partial t} + \nabla(h\mathbf{u}) = 0 \end{aligned} \quad (1)$$

where h is the total water depth, \mathbf{u} represents the depth-averaged horizontal velocity vector, \mathbf{f} is the Coriolis force, g is the gravitational acceleration, ν is the horizontally eddy-viscosity, ζ is the water level, ζ_{EQ} is the equilibrium

171 tide, ζ_{SAL} refers to the self-attraction and loading effect (SAL). The terms τ
 172 denote parameterizations of the friction stress. Most of the global tide energy
 173 dissipation comes from the bottom friction, and we use Chézy quadratic
 174 formulation with the coefficient of $77m^{1/2}s^{-1}$ in the model. Furthermore,
 175 internal tide friction is parameterized because there is approximately 1 TW
 176 energy dissipation, about 25 – 30% of the total, occurring in the deep ocean
 177 through internal wave drag (Maraldi et al., 2011). GTSM can also model
 178 surge using additional wind and air pressure conditions as the model forcing
 179 (Pugh and Woodworth, 2014).

180 We combined different datasets for the bathymetry. EMODnet bathymetry
 181 with a resolution of about 250m is implemented as the input of bathymetry
 182 in Europe. General Bathymetric Chart of the Ocean dataset (GEBCO 2019)
 183 with 15 arc-second resolution is used at the rest of the globe. However, there
 184 is still a large uncertainty in bathymetry because even though bathymetry
 185 can be measured directly, large areas of the oceans are unsurveyed and only
 186 estimated by satellite altimetry with a much lower effective resolution of
 187 8.9km (Weatherall et al., 2015; Tozer et al., 2019).

188 An essential characteristic of Delft3D-FM is unstructured grids (Kernkamp
 189 et al., 2011). The scale of tidal components is usually more prominent in the
 190 nearshore than in the deep ocean. High resolution is required in the coastal
 191 region to provide highly accurate modeling. Pringle et al. (2021) also re-
 192 ported that the mesh refinement in shallow waters, where the coast and at
 193 steep topography, is important for the global accuracy of the simulated as-
 194 tronomical tide.

195 Here, we use GTSM with two different resolutions (GTSM with the coarse
 196 grid and GTSM with the fine grid hereinafter). Table 1 reports the compu-
 197 tation time of the coarse and fine resolution models. As expected, GTSM
 198 with the fine grid has a longer computational time but more accurate tide
 199 forecasts. However, many fine model simulations needed in the parameter
 200 estimation procedure would require weeks or even months of computational
 201 time, which is unbearable.

202 3. Parameter Estimation with Model Order Reduction

203 3.1. Parameter Estimation Framework

204 We design an efficient and low-memory usage parameter estimation scheme
 205 with model order reduction for the high-resolution tide models to reduce pa-

Table 1: Computation time of the coarse and fine resolution GTSM models, measured for model simulation with a time length of 45 days and using 200 cores of Intel E5 processors on the Dutch National Supercomputer Cartesius. The model simulation time step is 5 minutes.

Model	GTSM with the coarse grid	GTSM with the fine grid
Resolution	deep ocean:50km coastal region:5km;	Europe:1.25km other coastal region: 2.5km
Cells	2 million	4.9 million
Computational time	25 minutes	70 minutes

parameter uncertainties and improve forecast accuracy. The flowchart of this parameter estimation scheme is shown in Figure 1.

The basic estimation algorithm applied here is called DUD (Doesn't use derivatives) in a generic data-assimilation toolbox OpenDA (Ralston and Jennrich, 1978; Karri et al., 2013). It optimizes the parameters by iteratively minimizing the following cost function:

$$J(x) = \frac{1}{2}(x - x_b)^T B^{-1}(x - x_b) + \frac{1}{2}[Y - H(x)]^T R^{-1}[Y - H(x)] \quad (2)$$

where Y is the field observation vector including all time steps in $t \in [t_1, t_{N_t}]$ and all stations $(1, \dots, N_s)$. x is the vector of parameters to be estimated, with the dimension of n . $H(x)$ is the model output vector matching observation locations for all time steps. x_b is the initial parameter vector. B and R are the background and observation error covariances, respectively. The dimension of observation Y and model output $H(x)$ in all space points and time steps is as $O(N_s \times N_t)$. The first term in the right hand of the cost function (Eqs. 2) is the background term J_b constraining the changes to the initial parameters. The second term is the observation term J_o representing the difference between model output and observations. For the brief introduction of the DUD algorithm and parameter estimation scheme, we only describe the observation term of the cost function in the following sections.

Figure 1 shows the flowchart of the parameter estimation scheme, connecting the components DUD, time-POD and outer-loop. DUD is implemented in the inner loop combining with the coarse-to-fine strategy and time-POD application. DUD is a Gauss-Newton similar algorithm but derivative-free. It started from the model simulation of first guesses for the parameters $x_0 = x_b$

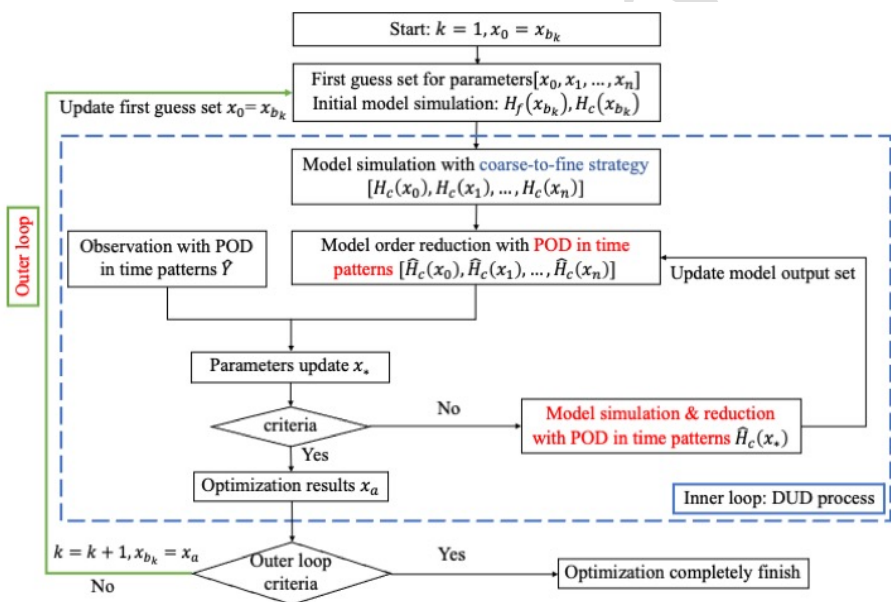


Figure 1: Flowchart of the iterative parameter estimation scheme to connect the components: DUD, time-POD and the outer-loop iteration. New approaches we proposed in this study are in color red.

and n simulations with each parameter perturbed as ($x_1 = x_b + \delta e_1, x_2 = x_b + \delta e_2, \dots, x_n = x_b + \delta e_n$). Parameter is updated for an approximate linear model that fits exactly through the model output for $[x_0, x_1, \dots, x_n]$. DUD iteratively finds the parameters that minimize the sum of squares between model output and observations.

We propose to improve estimation performance while reducing the computational cost and memory requirement based on the original DUD algorithm. There are several methods developed: the coarse-to-fine strategy, model order reduction in time patterns, and introduction of outer loop iterations.

In our previous study (Wang et al., 2021), a coarse-to-fine strategy called Coarse Incremental Calibration is proposed to reduce the computational cost. It is also applied here using a coarser grid model to replace the increments between the output from the initial model and the model with modified parameters. Term $H_f(x)$ and $H_c(x)$ are defined as the model output with the fine and coarse grid, respectively. $H_f(x)$ can be approximated with $H_f(x_b) + (H_c(x) - H_c(x_b))$, thus the cost function is represented as:

$$J_o(x) = \frac{1}{2}[Y - H_f(x_b) + H_c(x_b) - H_c(x)]^T R^{-1} [Y - H_f(x_b) + H_c(x_b) - H_c(x)] \quad (3)$$

Therefore, GTSM with the fine grid is only simulated to generate the initial model output $H_f(x_b)$. Other simulations in the inner iterations use GTSM with the coarse grid instead, which reduces the computing time to approximately 36% of the original.

In this research, we consider reducing the dimension of the model output by MOR. The dimension of model output $[H(x_0), H(x_1), \dots, H(x_{n+1})]$ and observations y is huge, which requires a huge memory, especially when the model has a long simulation time length. For example, if the number of observations N_s is $O(10^3)$, and with the number of time steps N_t is $O(10^3)$. Then, the dimension of the model output $H(x)$ and observations y is $O(10^6)$. If we assume the parameter dimension n is in the order of $O(10^2)$. The parameter dimension is the length of the vector with the parameters estimated. In this paper, we define spatial subdomains where a single multiplicative adjustment is applied. Each of these subdomains adds an element to the parameter vector. Thus, the dimension of the model output in the analysis step is $O(10^8)$, such a huge memory usage is unacceptable in practice. Therefore, we apply POD in the time patterns for model output and observations to reduce memory usage in the estimation procedure (that will be further explained in Section 3.2).

Moreover, we use the DUD process in the inner loop to obtain the updated parameters at a lower resolution (see Figure 1). With the Coarse Incremental Calibration approach, high resolution GTSM only plays a role as the initial output $H_f(x_b)$ in Eqs. 3 while instead by the coarse grid model $H_c(x)$ for iterative update. Even though our previous experiments demonstrate that coarse-grid increments can well represent the fine-grid increments (Wang et al., 2021), the results after the estimation can still be significantly affected by the model with the coarse grid. Therefore, we introduce the outer loop to take the high-resolution model states into account. The updated parameters obtained from the previous converged DUD process are used as the new first guess to update the initial model output. The cost function can be rewritten as:

$$J_o(x) = \frac{1}{2}[Y - H_f(x_{b_k}) + H_c(x_{b_k}) - H_c(x)]^T R^{-1}[Y - H_f(x_{b_k}) + H_c(x_{b_k}) - H_c(x)] \quad (4)$$

where k is the iteration number of the outer loop, x_{b_k} is set to be the optimized parameters $x_{a_{k-1}}$ from the previous DUD process. The estimation process terminates once the cost function has converged.

Compared to the computation-efficient parameter estimation scheme we proposed in the previous study (Wang et al., 2021), the estimation scheme in this paper also contributes to memory reduction with the time-POD algorithm and estimation accuracy improvement by the outer loop iterations. The combination of these methods gives a computation-efficient and memory-reduced parameter estimation framework.

The parameter estimation process with time-POD application and outer loops as shown in Figure 1 can be summarized as follows:

1. Define first guess parameter set $[x_0, x_1, \dots, x_n]$.
2. Analyze initial model output $H_f(x_b), H_c(x_b)$, determine the corresponding POD reduced model output $\hat{H}_f(x_b), \hat{H}_c(x_b)$ with the truncated basis matrix U_{N_p} .
3. Convert the original observations to corresponding observation \hat{Y} based on the truncated projection matrix.
4. Simulate the coarse grid model with the first guess parameter set, generate the POD reduced model states $[\hat{H}_c(x_0), \hat{H}_c(x_1), \hat{H}_c(x_2), \dots, \hat{H}_c(x_n)]$, and evaluate the cost function.

- 296 5. Find the new parameters x_* for an approximate linear model that fits
 297 exactly through the model output for $[x_0, x_1, \dots, x_n]$.
- 298 6. If the DUD stop criteria are not satisfied, then perform a model sim-
 299 ulation with updated parameters x_* and do model order reduction for
 300 model output $\hat{H}_c(x_*)$, and return to step 5.
- 301 7. If model outputs with optimization results don't reach the outer loop
 302 stop criteria, then return to step 1 with the optimized parameters as a
 303 new first guess for the next iteration of the DUD process.
- 304 8. Output: optimal estimation of parameters x_a in the last outer loop.

305 3.2. *Proper Orthogonal Decomposition (POD)*

306 In this section, details of the application of POD to reduce model di-
 307 mensions in time patterns are described. The time-POD reduced model is
 308 introduced first. Then, we define the corresponding observation term and
 309 error covariance. Finally, the complete parameter estimation procedure is
 310 summarized.

311 3.2.1. *Time-POD Reduced Model*

312 POD reduces the model order by identifying several modes with the most
 313 energies from a high-dimension system and uses these modes as a lower-
 314 dimension subspace approximation. Usually, the discrete POD is derived
 315 with snapshots to find a smaller subspace for states in spatial patterns. A
 316 snapshot is the value of the model state vector at a certain time. However,
 317 the vast memory requirement in our application comes from the model output
 318 $H_f(x)$, $H_c(x)$ and observation Y , containing the data both in space and time
 319 patterns in the order of $O(N_s N_t)$. As the simulation time increases, the
 320 dimension in time scale N_t is usually much larger than that in the spatial
 321 scale N_s . Thus, reducing the order in the time patterns is crucial. In the
 322 brief description of model order reduction below, we use $H(x)$ to represent
 323 the model output without considering the model resolution in this section.

324 In Section 3.1, $H(x)$ is a vector representing output in one model sim-
 325 ulation for all observation locations and time steps. To better explain the
 326 MOR applied to model output of time patterns, we rewrite the vector $H(x)$
 327 into a two-dimensional array $H_{N_t, N_s}(x) = [h^1(x), h^2(x), \dots, h^{N_s}(x)] \in \mathbb{R}^{N_t \times N_s}$
 328 to distinguish the time and space fields. $h^i(x)$ is the vector of model output

329 for all time steps at the i^{th} observation location. Now we want to find a pro-
 330 jection matrix $K \in \mathbb{R}^{N_t \times N_t}$ from \mathbb{R}^{N_t} to a smaller subspace which minimizes
 331 the error:

$$\|H_{N_t, N_s}(x) - KH_{N_t, N_s}(x)\|_2^2 = \Sigma_{i=1}^{N_s} \|h^i(x) - Kh^i(x)\|_2^2 \quad (5)$$

332 where an optimal orthonormal projection matrix K is given by:

$$K = U_{N_p} U_{N_p}^T \quad (6)$$

333 $U_{N_p} = [u_1, u_2, \dots, u_{N_p}] \in \mathbb{R}^{N_t \times N_p}$ is an orthogonal matrix containing the N_p
 334 eigenvectors of the correlation matrix $H_{N_t, N_s} H_{N_t, N_s}^T$ corresponding to the N_p
 335 largest eigenvalues, starting from the largest eigenvalue corresponding to u_1
 336 in decreasing order. The POD modes are the optimal ordered orthogonal
 337 matrix of basis vectors U_{N_p} in the least square sense. The truncated Singular
 338 Values Decomposition (SVD) is applied to derive the POD modes. It is the
 339 factorization of the matrix that generalizes the eigen decomposition via an
 340 extension of the polar decomposition:

$$H_{N_t, N_s}(x) = U \Sigma V^T \quad (7)$$

341 where, $U = [u_1, u_2, \dots, u_{N_t}] \in \mathbb{R}^{N_t \times N_t}$ and $V = [v_1, v_2, \dots, v_{N_s}] \in \mathbb{R}^{N_s \times N_s}$ are
 342 the orthogonal matrices, $\Sigma \in \mathbb{R}^{N_t \times N_s}$ is a diagonal matrix with rank r and
 343 diagonal value $\sigma_1, \sigma_2, \dots, \sigma_r$ are the singular values of H_{N_t, N_s} . Therefore, a new
 344 matrix \hat{H}_{N_p, N_s} can be defined by projecting the model output onto a smaller
 345 subspace using the truncated orthogonal matrices U_{N_p} , it is:

$$\hat{H}_{N_p, N_s}(x) = U_{N_p}^T H_{N_t, N_s}(x) \in \mathbb{R}^{N_p \times N_s} \quad (8)$$

346 We define the truncated orthogonal matrices $U_{N_p} \in \mathbb{R}^{N_t \times N_p}$ by keeping
 347 the first N_p columns of the matrix U , which correspond to the N_p modes
 348 with the highest energy of the dynamic system. In general, $\hat{H}_{N_p, N_s}(x)$ has
 349 a much smaller dimension compared to the model output $H_{N_t, N_s}(x)$, while
 350 retains the most important features. After the time-POD application, the
 351 two dimensional matrix $\hat{H}_{N_p, N_s}(x)$ is reshaped into the vector $\hat{H}(x)$ with a
 352 dimension of $O(N_p N_s)$:

$$\hat{H}(x) = \begin{bmatrix} U_{N_p}^T h^1(x) \\ U_{N_p}^T h^2(x) \\ \vdots \\ U_{N_p}^T h^{N_s}(x) \end{bmatrix} \quad (9)$$

³⁵⁵ $\hat{H}(x)$ is defined as the reduced model output vector used for the parameter
³⁵⁶ estimation process.

³⁵⁷ 3.2.2. Observation Term Conversion

³⁵⁸ In Section 3.2.1, the order of model output has been reduced to a cor-
³⁵⁹ responding model $\hat{H}_{N_p, N_s}(x)$ with a set of data identified on time patterns
³⁶⁰ instead of the real time-series. To match the model output matrix formula,
³⁶¹ we denote a two-dimensional array $Y_{N_t, N_s} = [y^1, y^2, \dots, y^{N_s}] \in \mathbb{R}^{N_t \times N_s}$ as the
³⁶² observation term that y^i is a vector containing time series in i^{th} location, we
³⁶³ have:

$$\hat{Y}_{N_p, N_s} = U_{N_p}^T Y_{N_t, N_s} \quad (10)$$

³⁶⁴ The truncated basis matrix U_{N_p} used here is from the initial model since
³⁶⁵ both the model and observations have a strong resemblance to the tidal
³⁶⁶ constituents in time patterns. The projection and reconstruction accuracy is
³⁶⁷ further analyzed in Section 5.1.1. The reduced observation vector \hat{Y} is:

$$\hat{Y} = \begin{bmatrix} U_{N_p}^T y^1 \\ U_{N_p}^T y^2 \\ \vdots \\ U_{N_p}^T y^{N_s} \end{bmatrix} \quad (11)$$

³⁶⁸ The observation error term has to be identified corresponding to the re-
³⁶⁹duced observation term. We define the statistic of observation error at i^{th}
³⁷⁰ location over all time steps as follows:

$$R^i = E([y^i - E(y^i)][y^i - E(y^i)]^T) \quad (12)$$

³⁷¹ where $E(y^i) = y_t^i$ is a vector of the truth at all discrete times at location i .
³⁷² The POD based observation error covariance \hat{R}^i is:

$$\begin{aligned} \hat{R}^i &= E([\hat{y}^i - \hat{y}_t^i][\hat{y}^i - \hat{y}_t^i]^T) \\ &= E([U_{N_p}^T y^i - U_{N_p}^T y_t^i][U_{N_p}^T y^i - U_{N_p}^T y_t^i]^T) \\ &= U_{N_p}^T R^i U_{N_p} \end{aligned} \quad (13)$$

³⁷³ In this application, we assume observation error is time invariant. The
³⁷⁴ covariance matrix R^j is a diagonal matrix with σ^2 as diagonal values (σ is

375 the observation uncertainty and we set its value as $0.05m$ in this applica-
 376 tion), so $R^j = \sigma^2 I_{(N_t)}$. Therefore, after the model order reduction, the new
 377 observation error covariance for location i is $\hat{R}^j = \sigma^2 I_{(N_p)}$. \hat{R} is the diagonal
 378 matrix including observation error covariance at all observation locations.
 379 We rewrite the cost function with the order reduced model output and ob-
 380 servation terms as follows:

$$J_o(x) = \frac{1}{2} [\hat{Y} - \hat{H}_f(x_{b_k}) + \hat{H}_c(x_{b_k}) - \hat{H}_c(x)]^T \hat{R}^{-1} [\hat{Y} - \hat{H}_f(x_{b_k}) + \hat{H}_c(x_{b_k}) - \hat{H}_c(x)] \quad (14)$$

381 4. Experiment Configuration

382 In this section, we describe the experiment configuration, including the
 383 parameter selection, model setup, observations, and the setup of three ex-
 384 periments.

385 4.1. Parameters with Uncertainties

386 Bathymetry is known as the parameter with the largest uncertainties
 387 for GTSM, especially in deep oceans, compared to bottom friction and in-
 388 ternal tides drag coefficient (Wang et al., 2021). Constrained by limited
 389 observations, computational sources, and storage memory, it is very hard to
 390 accurately estimate the bathymetry in over $O(10^6)$ grid cells. To reduce the
 391 parameter dimension, we partitioned the global ocean into 110 subdomains
 392 based on the study of tide propagation length and bathymetry sensitivity test
 393 results (Wang et al., 2021). A specified correction factor with uniform values
 394 is defined for each subdomain. The equation for adjusting the bathymetry
 395 in the subdomain $S_i, i = 1, \dots, n$ is:

$$D_j^* = (1 + [x]_i) D_j \text{ for } j \in S_i \quad (15)$$

396 where D_j is the bathymetry of the j^{th} grid in the subdomain S_i and $[x]_i$ is the
 397 i^{th} element of the parameter vector x . The initial guess for each parameter
 398 element is zero. In this study, the parameter x comprises the bathymetry
 399 correction factors in the 110 subdomains. For instance, if $[x]_1 = 0.05$, the
 400 bathymetry in region S_1 will be increased by 5%. By assuming a constant
 401 adjusting correction factor in each subdomain, the parameter dimension is
 402 reduced to an acceptable size. Parameter uncertainties are defined as 5%.

403 To ensure a realistic bathymetry estimation, we impose three constraints
 404 for the experiments. Firstly, using the background term $\frac{1}{2}(x - x_b)^T b^{-1}(x -$
 405 $x_B)^T$ in the cost function as the weak constraint to prevent the adjusted
 406 parameter departs far away from the original values while only improving
 407 the estimate a little. Secondly, a two-degree transition area is applied be-
 408 tween neighboring subdomains to avoid the correction factor jumps between
 409 different subdomains. Values for each grid cell in the transition areas are
 410 automatically interpolated by the model, leading to smoother correction fac-
 411 tors around the partition boundary. Thirdly, a hard constraint of 10% is set
 412 for all parameters to ensure the changes are kept between -10% and 10%.

413 4.2. Model Set-up

414 In this study, GTSM calibration is only based on the tide representation
 415 for two reasons. Firstly, it is not easy to obtain globally distributed surge
 416 observations, and the FES2014 dataset we used only provides tidal compo-
 417 nents. Secondly, surge is more sensitive to the wind and air pressure but
 418 less to the bathymetry. Wang et al. (2021) demonstrated it by comparing
 419 the surge simulation after the bathymetry estimation to the initial model
 420 with the UHSLC dataset. After the estimation, the water level forecast is
 421 improved from the higher tide forecast accuracy, and the changes of surge
 422 simulation are not significant. Thus, we use the tide representation of GTSM
 423 for bathymetry estimation. GTSM is forced by the tidal potential, with the
 424 Doodson number ranging from 57.565 to 375.575. We set the minimum
 425 threshold for the tidal spherical harmonic amplitude to 0.03m, leading to a
 426 set of 58 tidal generating frequencies. Long-term tide components SA and
 427 SSA are removed from the tidal frequencies because they are still affected by
 428 non-gravitational influences. Estimation accuracy is strongly related to the
 429 simulation time length used in the estimation procedure. In principle, it has
 430 to be long enough, such as a month or even a year, to capture the essential
 431 tide frequencies. However, available computer memory cannot store the large
 432 amount of model output from many simulations with long simulation time
 433 lengths in the iterative optimization algorithm. A previous experiment se-
 434 lects one spring-neap cycle (14 days), which fits into the memory of 32Gb on
 435 our cluster. However, experiment results showed the problem of over-fitting
 436 due to the insufficient simulation time length (Wang et al., 2021).

437 In the current experiments, we use a simulation time of two weeks, be-
 438 tween 1 to 14 January 2014, to compare the estimation performance with
 439 and without the time-POD model reduction. After that, the final model

440 estimation covers the simulation of two spring-neap cycles (1 month) with
 441 time-POD and outer loop application. Therefore, the simulation starts from
 442 1 to 31 January 2014 with a two-week spin-up before January 1. The time
 443 interval is set as 10 minutes, which results in 4465 time steps.

444 *4.3. Observation Network for Calibration and Validation*

445 Our parameter estimation uses the tide series derived from the FES2014
 446 dataset in the deep ocean. Tide gauge data from the University of Hawaii
 447 Sea Level Centre (UHSLC) is applied for the model validation (Caldwell and
 448 Thompson, 2015).

449 The FES2014 dataset comes from the FES (Finite Element Solution) tide
 450 model consisting of about 2.9 million nodes (Carrere et al., 2013). Long al-
 451 timeter time series, tide gauges, improved modeling, and data assimilation
 452 techniques have provided an accurate solution for FES2014. FES2014 per-
 453 forms better than GTSM when comparing with Deep-Ocean Bottom Pressure
 454 Recorder data (Wang et al., 2021; Stammer et al., 2014). And FES2014 has
 455 an advantage in deep ocean calibration because its ease of obtaining arb-
 456 itrary time series and locations globally. Therefore, the FES2014 dataset is
 457 selected as the observations for model calibration. 1973 time series with 32
 458 tide constituents (excluding long-term constituents SA and SSA) are derived
 459 from the FES2014 dataset for the model calibration. These 1973 locations
 460 are almost evenly distributed in the ocean.

461 The UHSLC dataset is a collection of approximately 500 distributed tide
 462 gauge time series covering different years across the globe. The specific
 463 amount of available data varies over the years. Two levels of quality con-
 464 trol, Fast Delivery (FD) and Research Quality Data (RQD), are provided in
 465 the UHSLC dataset. Tide gauges are somewhat irregularly distributed, and
 466 most of them are in the coastal regions, which leads the data more suitable
 467 for model validation than global model calibration. We retrieved the 283 tide
 468 gauge series from the hourly RQD in the year 2014. After the tide analysis
 469 with tidal analysis software (TIDEGUI) and visual inspection of the tide and
 470 surge representations against the measured series in the tide analysis proce-
 471 dure, tide representations with a set of 93 components from 230 tide gauge
 472 stations are finally used for the model validation.

473 It is worth noting that long-term tidal constituents SA and SSA are re-
 474 moved from FES2014 and UHSLC tide representations to ensure the consis-
 475 tency between observations and model output. Also, even though some tide
 476 gauge data are assimilated in the FES2014 dataset, It is still reasonable to

Table 2: Experiments set-up

Name	Simulation time ^a	Time steps	Outer loop	POD	Modes size	Data size before POD	Data size after POD
EX1	1-14 Jan.	2017	No	No	N/A	3.32Gb	N/A
EX2	1-14 Jan.	2017	No	Yes	200	3.32Gb	0.33Gb
EX3	1-31 Jan.	4465	Yes	Yes	200	7.35Gb	0.33Gb

^a Experiments are performed in the year of 2014.

477 assume that FES is independent of UHSLC data. On the one hand, most
 478 of the tide gauges are in the coastal regions, while the 1973 time series we
 479 derived are for the deep ocean. On the other hand, UHSLC data in this ap-
 480 plication is used to evaluate the estimated model performance in the coastal
 481 regions.

482 4.4. Experiments Set-up

483 Three experiments are set up to investigate the performance of the time-
 484 POD parameter estimation scheme for GTSM, as Table 2 shows. EX1 is
 485 the experiment with a short simulation time of two weeks without POD im-
 486 plementation and the outer loop. It is very similar to the experiment in
 487 Approach 2 of Wang et al. (2021). The memory needed for the total model
 488 output in this scheme to estimate 110 parameters is approximately 3.5Gb.
 489 EX2 has the same settings as EX1 but with the implementation of POD. It
 490 aims to evaluate the influence on the accuracy by applying POD, the memory
 491 use is significantly reduced when compared to EX1. Finally, the experiment
 492 denoted as EX3 follows the parameter estimation scheme in Figure 1, cover-
 493 ing a 1-month simulation time length from 1 to 31 January 2014. Without
 494 MOR, the data size of $[H_c(x_0), H_c(x_1), \dots, H_c(x_n)]$ and observation was about
 495 7.35Gb, and the total memory use was more than 20Gb for this experiment.
 496 With the proposed POD approach, the memory use is sharply reduced to
 497 4.5% after the POD application.

498 5. Numerical Experiments and Results

499 To assess the performance of POD, we first evaluate the projection and
 500 reconstruction accuracy of the model output and observations, followed by a
 501 comparison of results between EX1 and EX2. Last, the estimation results in
 502 EX3 are analyzed.

503 *5.1. POD Performance Analysis*

504 *5.1.1. Reconstruction Accuracy*

505 The accuracy of parameter estimation with MOR depends on the recon-
 506 struction accuracy of the model output and observations. The reconstructed
 507 model output and observation terms are in the formula of $U_{N_p} U_{N_p}^T H_{N_s, N_t}(x)$
 508 (the term $KH_{N_s, N_t}(x)$ in Eqs.5) and $U_{N_p} U_{N_p}^T Y$. The basis matrix U_{N_p} is
 509 obtained by truncated SVD from the initial model output or observations.
 510 Figure 2 shows the Root Mean Square Error (RMSE) between the original
 511 and the reconstructed model output (observation) with different number of
 512 modes. Time series is from 1 to 31 January 2014.

513 In general, the RMSE is decreased with the increase of the truncation
 514 size. Basis matrix from observation (Figure 2c) shows slower downtrends
 515 than others (Figure 2a, 2b). One possible reason is the model has more tidal
 516 components that are not included in the observations, there are 32 tidal
 517 constituents in observations while 58 tide potential frequencies are in the
 518 model. But that will not affect the estimation results because the RMSE
 519 for reconstructed model and observations without truncation is less than
 520 $5 \times 10^{-4} m$. It means the missing components in observation would lead
 521 to at most $5 \times 10^{-4} m$ water level changes while the observation error we
 522 defined is $0.05 m$, which is 100 times larger. Figure 2a shows the excellent
 523 accuracy of the reconstructed coarse model. The reconstructed fine model
 524 and observations have similar performance when the truncation size varies.
 525 Figure 2b is opposite to Figure 2a for the coarse model. We use the basis
 526 matrix from the coarse model with 200 modes for the calibration process
 527 because most of the model simulation in the estimation iteration is on the
 528 coarse grid. Reducing the coarse model output with 200 modes sharply
 529 reduces the data size, while the high accuracy for the coarse model with
 530 RMSE of $2.64 \times 10^{-4} m$ is attained and the reconstructed observation error
 531 is also smaller than the observation uncertainty.

532 Tidal analysis can also be used to reduce the data size, but in compari-
 533 son, the time-pattern projection has two advantages. Firstly, tidal analysis
 534 requires the selection of a set of tidal constituents. These constituents should
 535 respect the Rayleigh criterion. The projection method has only one param-
 536 eter to which is quite insensitive. For example, time-series of reconstructed
 537 model output and observations for modes 1 to 3 (Figure 3a-3c) in an obser-
 538 vation location provide similar waves to the harmonic, implying the patterns
 539 in the projection method work similarly as the tide analysis does but without

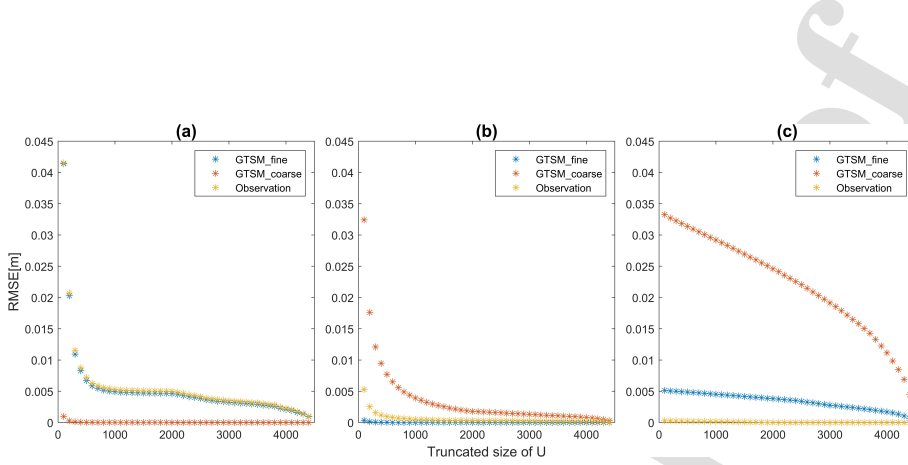


Figure 2: RMSE between the initial model output $H(X)$ and reconstructed model output $\hat{H}(x)$ for various truncation sizes (unit: m). With the projection basis vectors derived from (a) initial coarse model; (b) initial fine model; (c) observations.

Table 3: The amplitude of eight major tide components from tide analysis for the time-series of the original GTSM with fine grid and the projection on mode 1-3 for the arbitrary location in (cm): (-70.1110, -23.1397).

Components	Q1	O1	P1	K1	N2	M2	S2	K2
GTSM with fine grid	7.2	26.06	7.18	21.89	6.34	46.74	33.73	9.58
Projection on mode 1	0.22	1.73	0.77	2.35	8.54	40.92	12.10	3.44
Projection on mode 2	0.23	0.53	0.30	0.90	5.51	26.10	8.05	2.29
Projection on mode 3	4.89	15.33	6.96	21.21	0.80	2.31	1.92	0.54

the restriction to separating the independent tide components. Secondly, the projection method gives almost identical results to the time-series approach. The reconstructed fine grid model output with projection on the first three modes (Figure 3d) is close to the original data. When more modes (200 modes we selected) are included, the reconstruction error would become very small. We also performed a tidal analysis for the time series from the model output for this location and after projection onto modes 1- 3, as shown in Table 3. The projection on modes 1 and 2 mainly shows large amplitudes for the semi-diurnal tides (N2, M2, S2, K2). The contributions from N2 and M2 add up to a large part of the N2, M2 signal, while this is a bit less for S2 and K2. Mode 3 mainly shows diurnal constituents, where the P1 and K1 amplitudes are close to the values for the full signal. The time projection thus shows some resemblance to tidal analysis.

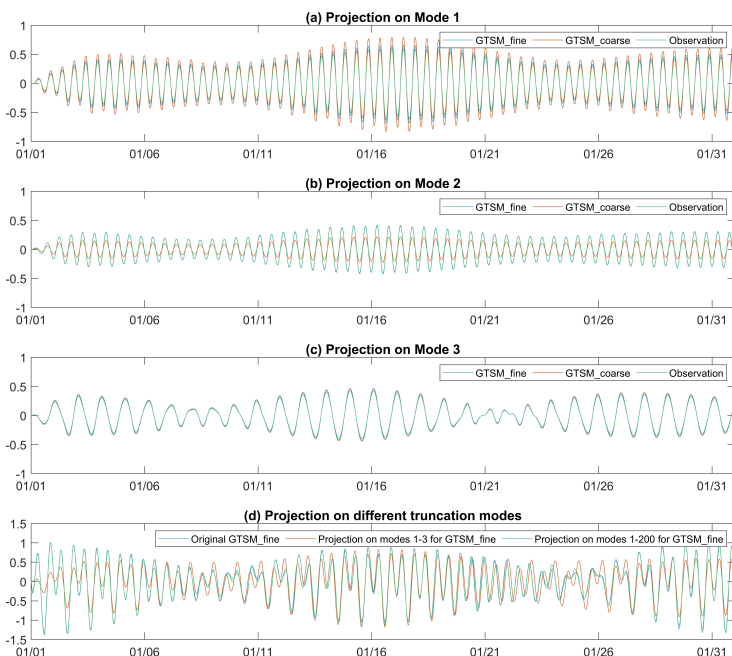


Figure 3: Time series of the model output and observation with projection in the observation location (-70.1110,-23.1397). (a) Projection on Mode 1; (b) Projection on Mode 2; (c) Projection on Mode 3; (d) Projection on different truncation modes.

553 *5.1.2. Experiments with Time-POD Application*

554 Figure 4 shows the cost function (Figure 4a) and optimized bathymetry
 555 correction factors of EX1 (Figure 4b) and EX2 (Figure 4c). EX2, estimation
 556 with time-POD, shows a similar behavior of the cost function in each iter-
 557 ation as EX1 and nearly the same correction factors. The RMSE for both
 558 experiments decreases from 5.23cm to 3.49cm in the calibration period, while
 559 the required memory in EX2 is reduced by a factor of 10.

560 Figure 5 illustrates the the difference of RMSE at different observation
 561 locations between the initial model and the estimated model in EX2 (i.e.,
 562 RMSE between the initial model and observations - RMSE between the es-
 563 timated model and observations). It reports nearly the same improvement
 564 after the estimation as in EX1 (not shown here). Therefore, model order re-
 565 duction is an efficient approach to reduce memory requirements for parameter
 566 estimation without causing any loss of estimation accuracy.

567 The purpose of parameter estimation is to improve the GTSM long-term
 568 forecast accuracy. However, the interaction of tidal constituents varies during
 569 different periods. For example, the RMSE between estimated model output
 570 and observations is 3.49cm from 1 to 14 January, while the RSME in the fore-
 571 cast increases to 4.33cm for the period from 15 to 31 January 2014. A short
 572 simulation time length would lead to over-fit the data in the estimation pe-
 573 riod (Wang et al., 2021). After assessing model order reduction performance,
 574 we selected a longer simulation time of 1 month and experimented in Section
 575 5.2.

576 *5.2. Parameter Estimation Results Analysis*

577 EX3 covers a simulation time length of 1 month for GTSM to estimate
 578 bathymetry. Figure 6a illustrates the changes in the cost function in each
 579 simulation in the three outer loop iterations. In every outer loop, the cost
 580 functions of the first 111 runs include one initial simulation and 110 indepen-
 581 dent simulations each corresponding to perturbing one of the 110 parameters.
 582 Parameters are iteratively updated after the first 111 simulations. The sim-
 583 ulation experiment was run using 200 cores for about 12 days, with a total
 584 of approximately 57600h CPU times.

585 In the first outer loop (color red in Figure 6a), the cost function has a
 586 sharp reduction from 7.21×10^6 to 3.17×10^6 and then slowly reduced to
 587 3.00×10^6 at the end of the second outer loop (color blue). Compared with
 588 the first outer loop, the cost function in the second outer loop only reduces
 589 slightly. It looks that the estimation results are converged to a certain value.

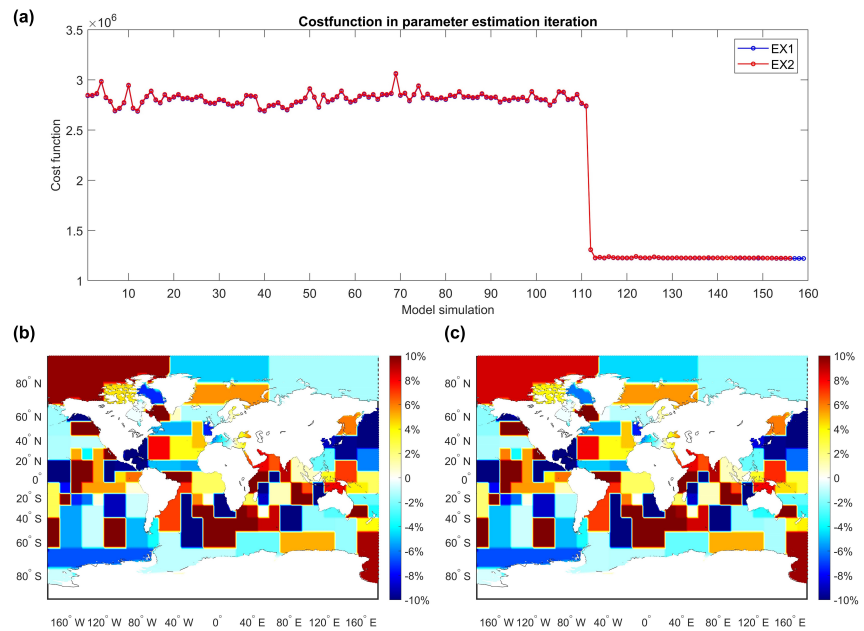


Figure 4: (a) Cost function in EX1 and EX2. Relative adjustments of Bathymetry as estimated in EX1 (b) and EX2 (c). Positive values show a deepening.

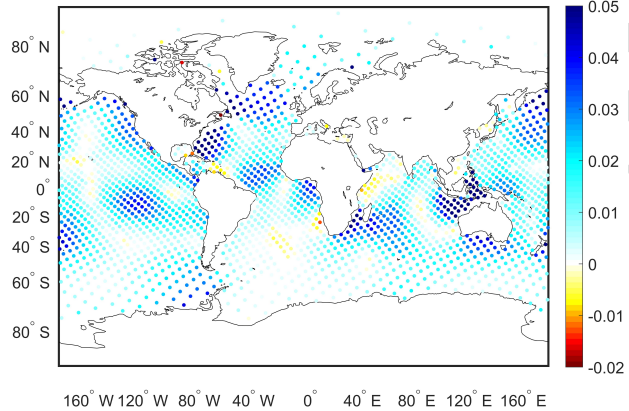


Figure 5: RMSE difference between the initial model and estimated model in EX2 in the period from 1 to 14 January 2014, color blue shows the improvement. [unit:m]

590 In the third out loop, the difference of cost functions in each simulation
 591 is very slight, making the DUD process difficult to continue, leading to a
 592 stop after several iterations with a value of 2.95×10^6 . It is in the same
 593 magnitude as that in the second outer loop. GTSM parameter estimation
 594 is converged in the third outer loop iteration. Moreover, sensitivity for each
 595 parameter can be observed from the variability of the cost function for the
 596 initial 111 perturbation runs in each outer loop. This is strongly decreased
 597 in the third outer loop, indicating that the estimated parameters are close
 598 to the minimum. The final relative change to the bathymetry, which is the
 599 correction factor $[x]$ in Eqs. 15 is shown in Figure 6b. The value varies
 600 between -0.1 to 0.1 within the range of hard constraints.

601 Estimation performance is analyzed by comparing the model output with
 602 the FES2014 dataset. For the comparison of the model performance in EX3
 603 and EX1, RMSE of two time periods is summarized in Table 4. RMSE is used
 604 to represent the difference between model output and observations to access
 605 model performance. The bias difference between model and observations
 606 is negligible (not shown here). As expected, GTSM with the fine grid has
 607 better performance than that with the coarse grid. Comparing the coarse
 608 grid GTSM, EX3 works better than EX1 in all outer loops and time periods.
 609 In the fine grid GTSM, EX1 performs slightly better than EX3 in the period

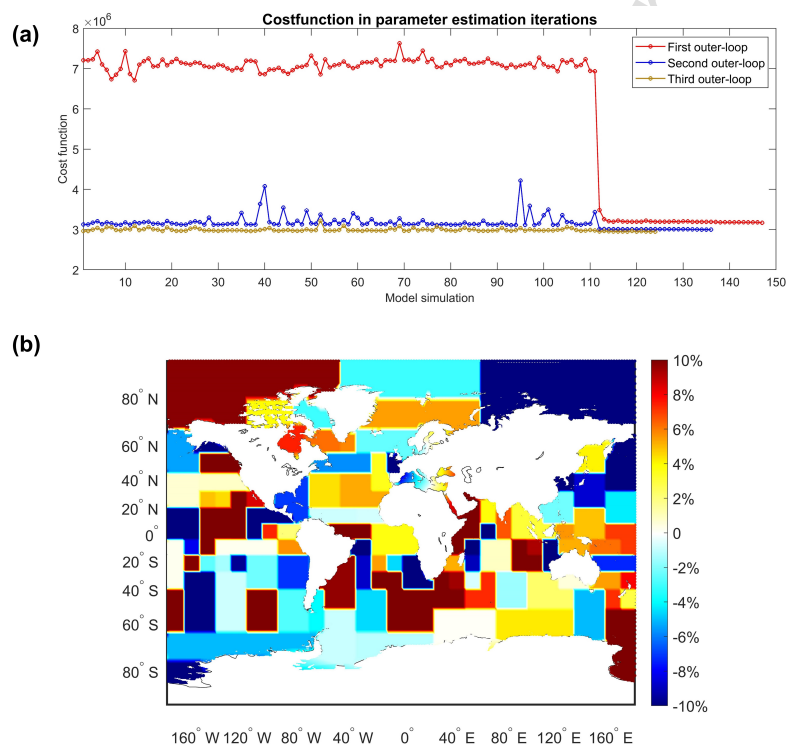


Figure 6: (a) Changes of the cost function values in the three outer loop iterations of EX3; (b) Relative adjustments of the bathymetry as estimated in EX3; Positive values show a deepening.

Table 4: RMSE between GTSM and FE2014 datasets in difference time periods [cm]

Model	Time period	Initial	EX1	EX3_1 ^a	EX3_2 ^a	EX3_3 ^a
GTSM with the coarse grid	1-14 Jan.	6.47	4.19	4.08	4.02	4.06
	15-31 Jan.	7.14	5.20	4.53	4.39	4.41
GTSM with the fine grid	1-14 Jan.	5.23	3.49	3.67	3.62	3.62
	15-31 Jan.	5.84	4.33	3.80	3.66	3.66

^a EX3_1, EX3_2, and EX3_3 represent the first, second, and third outer loop.

610 1 to 14 January but worse in 15 to 31 January 2014. This can be explained
 611 that EX1 estimates with a two-week simulation time (1 to 14 January 2014)
 612 resulting in an over-fitting of data in the calibration period. The RMSE
 613 is reduced from 5.23cm to 3.49cm in the period 1 to 14 January, while the
 614 reduction in the period 15 to 31 January is clearly less, from 5.84cm to 4.33cm
 615 in the 15 to 31 January. With a longer simulation time length of 1 month in
 616 EX3, the RMSE of the estimated fine model in these two periods is close to
 617 each other, namely 3.62cm and 3.66cm, implying the overfitting is reduced.
 618

619 The spatial distribution of RMSE for the fine GTSM in January is shown
 620 in Figure 7. Figure 7a is the RMSE between the estimated fine grid model
 621 output in EX3 and FES2014 observations. The differences of RMSE between
 622 the model before and after the estimation are shown in Figure 7b. It can be
 623 observed that the estimated model has been significantly improved in most
 624 regions. A few areas that are not improved or a bit worse than the initial
 625 model, see the areas with yellow colors (negative values of RMSE difference)
 626 in Figure 7b. Possibly, not only bathymetry but also other effects such as
 627 the lack of resolution, play a role here. The regions getting worse only takes
 628 up a small part of the ocean; In addition, estimation by EX3 outperforms
 629 EX1 in most ocean sea, as Figure 7c shows. Generally, the estimated model
 significantly overperforms the initial model.

630 In summary, the calibrated model in EX3 is in better agreement with
 631 the measurements than EX1. Model order reduction reduces the memory
 632 requirement by a factor of 22 while keeping a better estimation accuracy.
 633 Long simulation time is beneficial for parameter estimation in GTSM, and the
 634 implementation of the outer loop further improves the tide forecast accuracy.

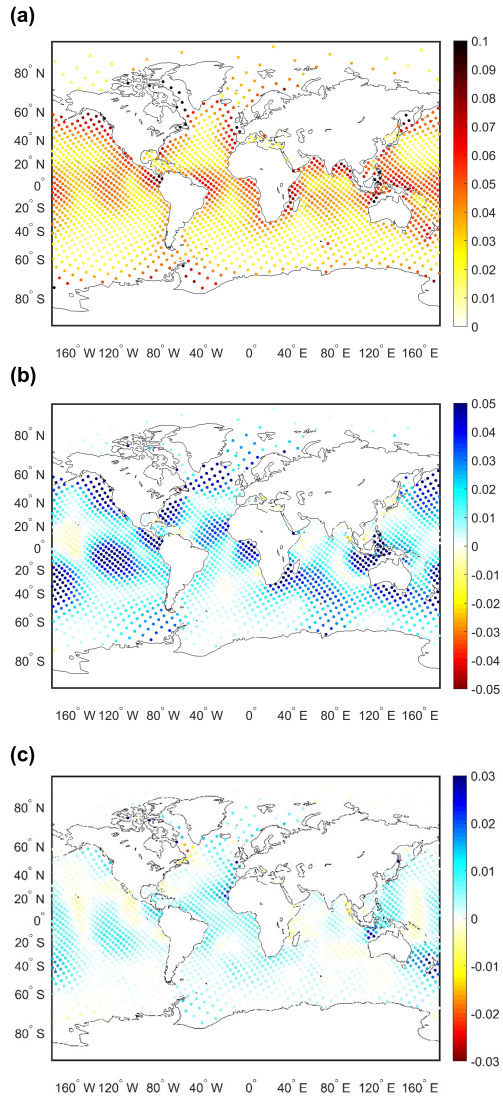


Figure 7: (a) RMSE between estimated fine grid GTSM in EX3 and FES2014 dataset in January 2014; (b) Difference of RMSE between the initial model and the estimated model, color blue shows the improvement; (c) Difference of RMSE between model after estimation in EX1 and EX3, color blue shows EX3 outperforms EX1. [unit: m]

635 **6. Model Validation**

636 To validate the model performance more independently from the simu-
 637 lation period and data we used in the estimation procedure. We analyzed
 638 the tide components from GTSM and compared them against the FES2014
 639 dataset in the frequency domain. The tide forecast of GTSM for the whole
 640 year of 2014 is also compared with observations from the FES2014 and UH-
 641 SLC datasets.

642 *6.1. Tide Analysis Comparison against FES2014 Dataset for 2014*

643 Model performance is evaluated in the frequency domain. Tide forecast
 644 from GTSM in the year 2014 for 1973 observation locations is analyzed with
 645 TIDEGUI software. We use the Root-mean-square (RMS) to assess the dif-
 646 ference between model output and observations for major tide components,
 647 with the formula:

$$RMS = \sqrt{\overline{(A_m \cos(\omega t - \phi_m) - A_o \cos(\omega t - \phi_o))^2}} \quad (16)$$

648 The term A_m and A_o are the amplitudes from model output and observations,
 649 respectively. ϕ_m, ϕ_o are terms of phases lag. ω is the tide frequency. The
 650 overbar shows the computation over one full cycle of the constituent (ωt
 651 varying from 0 to 2π) in all locations. Detailed results for 8 major tide
 652 components are summarized in Table 5. Root-sum-square (RSS) for these 8
 653 constituents is also analyzed.

654 It can be observed that RSS and RMS for all 8 major components are
 655 reduced after the estimation in EX1 and three outer loop iterations of EX3
 656 when comparing with the initial model. After the estimation, M2 is the com-
 657 ponent that significantly improved in EX3 reduced from 4.50cm to 1.89cm
 658 whereas it is 2.54cm in EX1. The other 7 components in EX3 are nearly
 659 the same or slightly better than that in EX1. The RSS over these eight
 660 components in EX3 is sharply reduced from 6.05cm to 3.52cm.

661 The differences in the amplitude and phase between the model output and
 662 FES2014 dataset for M2 component is shown in Figure 8. The difference in
 663 amplitudes and phases compared to FES2014 dataset is much smaller for the
 664 estimated models in EX1 and EX3 than for the initial model. EX3 has a
 665 better agreement with FES2014 dataset than EX1, especially in the phase
 666 domain (Figure 8e, 8f), consequently EX3 has a smaller RMS than EX1.

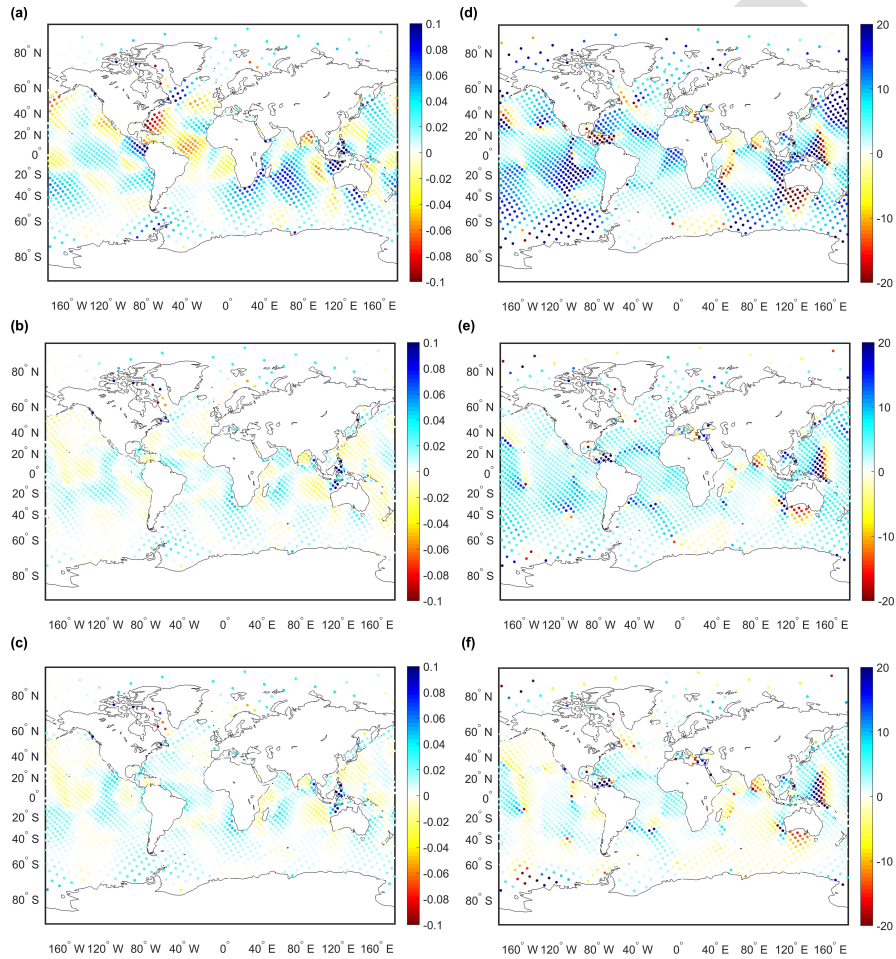


Figure 8: Spatial distribution of amplitudes and phase difference of M2 between model and FES2014 dataset. (a) (b) (c): Amplitudes difference for initial GTSM, model estimated in EX1 and EX3, respectively [unit: m]. (d) (e) (f): Phases difference for initial GTSM, model estimated in EX1 and EX3, respectively [unit: degree].

Table 5: RSS and RMS of eight major tide components between the fine GTSM and FES2014 dataset in (cm)

Components	RMS for all locations								RSS
	Q1	O1	P1	K1	N2	M2	S2	K2	
Initial	0.48	1.12	0.55	1.62	1.01	4.50	2.79	1.76	6.05
EX1	0.44	0.96	0.41	1.18	0.66	2.54	1.91	1.46	3.92
EX3_1	0.46	1.00	0.45	1.31	0.62	2.02	2.00	1.42	3.68
EX3_2	0.46	0.99	0.43	1.25	0.61	1.91	1.90	1.39	3.53
EX3_3	0.46	1.00	0.43	1.25	0.62	1.89	1.89	1.38	3.52

667 Initial GTSM performs better in deep ocean comparing with Deep-Ocean
 668 Bottom Pressure Recorder (BPR) observation than most of the purely hydrodynamic models described in Table 3 of Stammer et al. (2014), but not
 669 as accurate as the assimilative tide models (Wang et al., 2021). In this
 670 study, GTSM is significantly improved after our parameter estimation to
 671 bathymetry in the deep ocean. It overperforms the purely hydrodynamic
 672 models, especially in the M2 constituent, but still not better than the assimilative tide models. This result is expected because firstly observation locations are limited in the estimation process, and secondly not only bathymetry
 673 but other effects such as resolutions, other parameters like bottom friction
 674 would also affect the model performance. However, compared to other tide
 675 models, GTSM after parameter estimation has the advantage to access the
 676 effect of sea level rise and climate changes because it can include surge simulation
 677 when meteorological forcing wind and air pressure additions are added.
 678 Therefore, the high accuracy tide representations also benefit the complete
 679 water level forecast.

683 6.2. Monthly Comparison against FES2014 Time Series for 2014

684 GTSM is also validated through long-term tide forecasts, showing the
 685 model performance in different time periods. Model forecast in the whole
 686 year of 2014 is firstly analyzed with the FES2014 dataset. Figure 9 shows
 687 the regional RMSE of the fine GTSM after the estimation in EX1 and EX3
 688 for each month of year 2014. The regional RMSE between GTSM with the
 689 fine grid and FES2014 dataset are shown in Figure 9a-g. The global average
 690 of RMSE in 1973 locations is shown in Figure 9h.

691 Compared to the initial model, the RMSE for all the regions is significantly reduced in EX1 and EX3. RMSE in EX1 is larger than that in EX3 in

693 the year 2014, except for some months in the Indian Ocean. Forecast results
 694 also report that estimation with a longer simulation length works better than
 695 that with a short time window When comparing the RMSE in EX1 and the
 696 first outer loop of EX3. As the number of outer loop iterations increases,
 697 the model performs better throughout 2014. The 1-year forecast comparison
 698 with the FES2014 dataset demonstrates the estimated model can be used for
 699 the high-accuracy long-term forecast.

700 One can also observe a seasonal pattern in the RMSE in Figure 9, both
 701 before and after the calibration. A possible reason is that tide constituents
 702 interact differently for different periods, leading to a large or small differ-
 703 ence between the data and the model for each month. After calibration,
 704 this seasonal pattern is smaller in EX3 than EX1, indicating long simulation
 705 time length can weaken it and result in a better agreement to model and ob-
 706 servations. However, it remains challenging to verify whether using a more
 707 extended time period such as one year can further improve the model accu-
 708 racy and eliminate over-fitting due to the excessive computational demand.
 709 But we see no clear signals of over-fitting problem in EX3, and the 1-month
 710 calibration provides sufficient calibration accuracy.

711 6.3. Monthly Comparison against UHSLC Time Series for 2014

712 In the following, the performance of GTSM is assessed using a dataset
 713 that is not used in the estimation stage. Model performance in the coastal
 714 areas is evaluated by comparing with the UHSLC dataset in 2014.

715 Figure 10 shows the monthly averaged RMSE in 2014 between model
 716 output and the UHSLC measurement. The RMSE before the estimation is
 717 approximately 12.5-14 cm in each month and it is reduced to about 10-11.5cm
 718 after the estimation in both EX1 and EX3. It indicates the bathymetry
 719 estimation for the deep ocean can improve the accuracy in the nearshore. As
 720 expected, the results in EX3 are better than in EX1. The difference between
 721 the three outer loops is not significant, but the second outer loop is slightly
 722 better than the third outer loop. It can also be observed from the mean
 723 RMSE of the whole year of 2014 (Figure 10), the second loop has a value
 724 of 10.84cm smaller than the third outer loop with 10.94cm. One possible
 725 reason is the bathymetry estimation mainly works on the deep ocean. After
 726 three outer loop iterations, the parameter estimation overfits a bit the deep
 727 water observation used in the calibration process. Also, some other effects,
 728 such as bottom friction, play a role in shallow waters, but they are left out

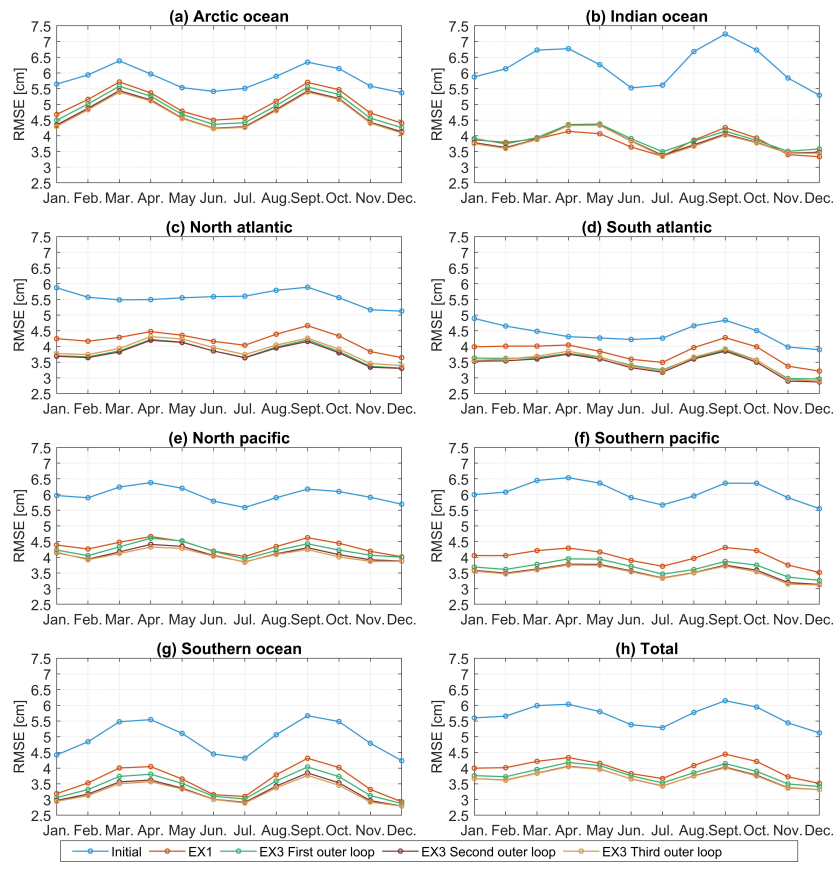


Figure 9: Regional RMSE between GTSM with the fine grid and FES2014 dataset in 2014.

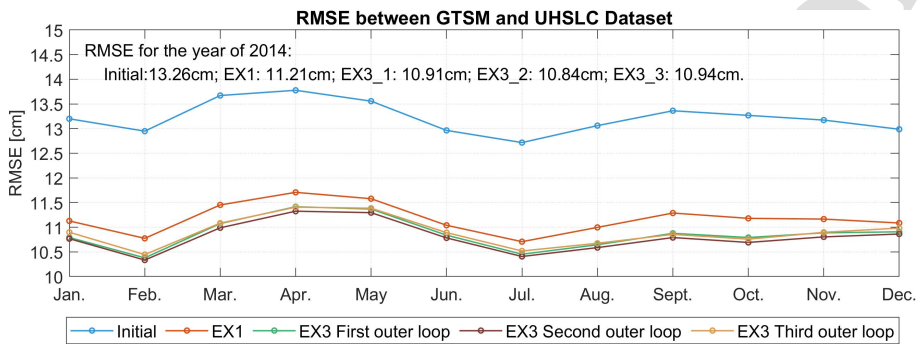


Figure 10: RMSE between GTSM with the fine grid and UHSLC dataset in 2014

of consideration in this study. Future works can continue on the parameter estimation for shallow waters.

Figure 11 shows the spatial distribution of RMSE between the initial fine model and UHSLC dataset in the year of 2014 (Figure 11a) and the RMSE difference between the model before and after estimation in EX3 (Figure 11b). Results in EX1 reported similar distribution as EX3 but with a slightly higher RMSE (not shown here). Most of the tide gauges are located in coastal areas with larger RMSE than deep oceans. After the global calibration, model performance near the coast is improved even though the calibration mainly focuses on the deep water.

To further have a closer look at the tide representation in one location, the time series of station Wellington Harbour in New Zealand is used as an example. Figure 12a shows the tide representation from the UHSLC dataset, the model output of the initial, EX1, and EX3. The difference between model output and observation is depicted in Figure 12b. The RMSE for the initial model is 15.25cm, and after the estimation in EX1, it is decreased by approximately 44.2% to 8.51cm. EX3, with the RMSE reduction of approximately 59.21%, is marginally better than in EX1.

The model validation for the whole year of 2014 shows excellent agreement with the FES2014 and UHSLC datasets in frequency and time domains after applying the memory-efficient estimation. It illustrates that GTSM with the adjusted bathymetry can provide high accuracy long-term tide forecast.

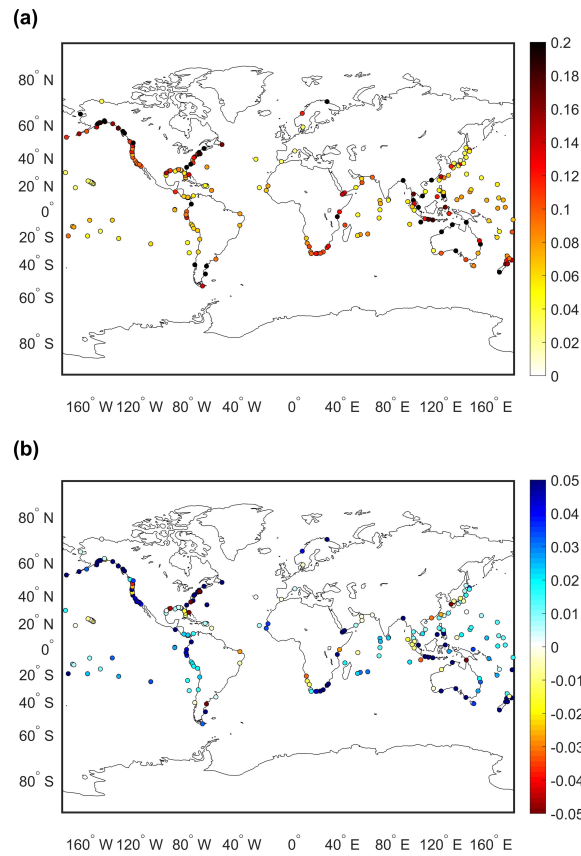


Figure 11: (a): RMSE between initial fine GTSM and UHSLC dataset in year 2014; (b): RMSE Difference between initial model and estimated model in EX3, color blue shows improvement.[unit:m]

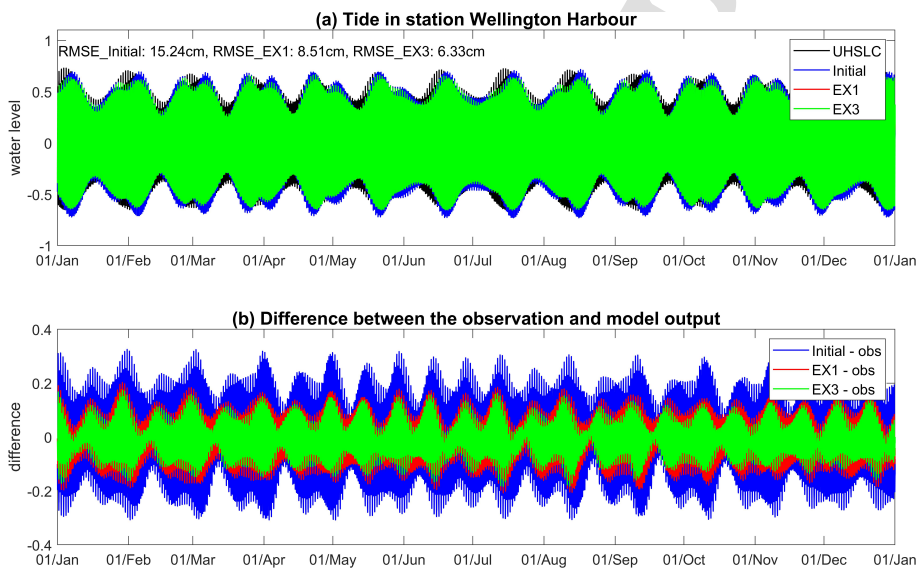


Figure 12: (a): Tide representation for station Wellington Harbour in year 2014; (b): Difference between different GTSM models with the fine grid and observation. Wellington Harbour is a location with coordinate of (-41.28,174.78) in the New Zealand.

751 7. Summary and Conclusion

752 This study presented a memory-efficient parameter estimation approach
 753 for the high-resolution global tide model over a long time length. To re-
 754 solve the memory constraint of the long period model simulation, time-POD
 755 model order reduction is developed to project the model output time patterns
 756 onto a smaller subspace. To further improve the model estimation accuracy
 757 with affordable computational cost, we implemented inner-outer loop iter-
 758 ations, similar to Incremental 4D-var, using an iterative parameter estimation
 759 algorithm called DUD in the inner loop with the lower-resolution model sim-
 760 ulation. The outer loop uses optimized parameters from the previous inner
 761 DUD process as a new reference run with the initial high-resolution model.
 762 This parameter estimation scheme is implemented for the Global Tide and
 763 Surge Model (GTSM) to correct bathymetry and substantially improve the
 764 model performance.

765 Our previous investigation showed that the accuracy of the calibrated
 766 model would probably benefit from a calibration period longer than the two
 767 weeks (one spring-neap cycle) used there, but the huge memory required was
 768 limiting an extension in practice (Wang et al., 2021). Here, we use time-POD
 769 model order reduction to project the GTSM output onto a limited number
 770 of time patterns. This projection reduces the memory usage by more than
 771 an order of magnitude in our experiments, while our experiments for GTSM
 772 show that parameter estimation with MOR achieves the same model accuracy
 773 as without MOR. This approach has the advantage of keeping the reduced
 774 model output size small when extending the simulation time length.

775 Finally, a parameter estimation experiment for GTSM with the imple-
 776 mentation of MOR and inner-outer loop iterations is performed. It covers
 777 a simulation time of 1 month while memory demand is reduced by a factor
 778 of 22 due to model order reduction for time fields. Experiment results show
 779 that the ocean tide is better represented in the calibration period. The cost
 780 function is converged within three outer loop iterations in this study. Model
 781 validation from the frequency domains illustrates the M2 component is sig-
 782 nificantly better estimated with the set-up of 1-month simulation length and
 783 the outer loop implementation. Model tide forecast in the whole year of 2014
 784 is compared with the FES2014 and UHSLC datasets. It demonstrates that a
 785 long simulation period in the estimation procedure improves the performance
 786 for long-term tide forecasting. The outer loop iterations contribute to further
 787 improvement of the model forecast but can lead to a bit of overfitting to the

788 data in the third outer loop.

789 In summary, parameter estimation leads to significant performance im-
 790 provements for GTSM. The memory requirements are significantly reduced,
 791 which allowed us to extend the time span used for calibration. This resulted
 792 in a more accurate reproduction of tides in GTSM. Bathymetry calibration
 793 contributes more to the deep ocean but also benefits a bit for shallow waters.
 794 Moreover, the time-POD parameter estimation is a general technique that
 795 can be widely used in many global or regional numerical models to estimate
 796 different parameters. Compared to harmonic analysis method, model simu-
 797 lation time length in time-POD estimation is not limited by the Rayleigh cri-
 798 terion. We have presented a case study of bathymetry estimation in a global
 799 tide and surge model. Even when only tide is simulated in the GTSM, the
 800 efficient estimation also benefits the complete water level forecasts including
 801 the tide and surge. In addition, this parameter estimation scheme can also be
 802 used to calibrate different parameters simultaneously (e.g., bathymetry, in-
 803 ternal tide friction and bottom friction combined), in particular, to estimate
 804 the bottom friction in shallow water with more tide gauge data.

805 Acknowledgement

806 The first author wishes to thank the China Scholarship Council for provid-
 807 ing financial support in terms of a scholarship grant. This work was carried
 808 out on the Dutch national e-infrastructure with the support of SURF. The
 809 FES2014 dataset was acquired from <https://www.aviso.altimetry.fr/>. Re-
 810 search Quality Data of UHSLC is made available at the University of Hawaii
 811 Sea Level Centre with the link <ftp://ftp.soest.hawaii.edu/uhslc/rqds>.
 812 Bathymetry data is available from https://www.gebco.net/data_and_products/gridded_bathymetry_data/ (GEBCO 2019) and <https://emodnet.ec.europa.eu/en/bathymetry>
 813 (EMODnet).

815 References

816 Antoulas, A., Ionutiu, R., Martins, N., Maten, ter, E., Mohaghegh, K., Pulch,
 817 R., Rommes, J., Saadvandi, M., Striebel, M., 2015. Model order reduction
 818 : methods, concepts and properties. CASA-report, Technische Universiteit
 819 Eindhoven.

- 820 Bannister, R.N., 2017. A review of operational methods of variational and
821 ensemble-variational data assimilation. Quarterly Journal of the Royal
822 Meteorological Society 143, 607–633.
- 823 Barth, A., Alvera-Azcárate, A., Gurgel, K.W., Staneva, J., Port, A., Beckers,
824 J.M., Stanev, E.V., 2010. Ensemble perturbation smoother for optimizing
825 tidal boundary conditions by assimilation of high-frequency radar surface
826 currents application to the german bight. Ocean Science 6, 161–178.
- 827 Beck, A., Ehrendorfer, M., 2005. Singular-vector-based covariance propaga-
828 tion in a quasigeostrophic assimilation system. Monthly Weather Review
829 133, 1295–1310.
- 830 Caldwell, P. C., M.A.M., Thompson, P.R., 2015. Sea level measured by tide
831 gauges from global oceans – the joint archive for sea level holdings (ncei ac-
832 cession 0019568), version 5.5. NOAA National Centers for Environmental
833 Information, Dataset .
- 834 Cane, M.A., Kaplan, A., Miller, R.N., Tang, B., Hackert, E.C., Busalacchi,
835 A.J., 1996. Mapping tropical pacific sea level: Data assimilation via a a
836 reduced state space kalman filter. Journal of Geophysical Research: Oceans
837 101, 22599–22617.
- 838 Cao, Y., Zhu, J., Navon, I.M., Luo, Z., 2007. A reduced-order approach
839 to four-dimensional variational data assimilation using proper orthogonal
840 decomposition. International Journal for Numerical Methods in Fluids 53,
841 1571–1583.
- 842 Carrere, L., Lyard, F., Cancet, M., Guillot, A., Roblou, L., 2013. FES 2012:
843 A New Global Tidal Model Taking Advantage of Nearly 20 Years of Al-
844 timetry, in: Ouwehand, L. (Ed.), 20 Years of Progress in Radar Altimetry,
845 p. 13.
- 846 Cazemier, W., Verstappen, R.W.C.P., Veldman, A.E.P., 1998. Proper or-
847 thogonal decomposition and low-dimensional models for driven cavity
848 flows. Physics of Fluids 10, 1685–1699.
- 849 Chatterjee, A., 2000. An introduction to the proper orthog-
850 onal decomposition. Current Science 78, 808–817. URL:
851 <http://www.jstor.org/stable/24103957>.

- 852 Chen, Y., Oliver, D.S., 2013. Levenberg–marquardt forms of the iterative
 853 ensemble smoother for efficient history matching and uncertainty quantifi-
 854 cation. Computational Geosciences 17, 689–703.
- 855 Courtier, P., Thépaut, J.N., Hollingsworth, A., 1994. A strategy for opera-
 856 tional implementation of 4d-var, using an incremental approach. Quarterly
 857 Journal of the Royal Meteorological Society 120, 1367–1387.
- 858 Daescu, D.N., Navon, I.M., 2008. A dual-weighted approach to order reduc-
 859 tion in 4dvar data assimilation. Monthly Weather Review 136, 1026–1041.
- 860 Das, S.K., Lardner, R.W., 1991. On the estimation of parameters of hydraulic
 861 models by assimilation of periodic tidal data. Journal of Geophysical Re-
 862 search: Ocean 96, 15.
- 863 Edwards, C.A., Moore, A.M., Hoteit, I., Cornuelle, B.D., 2015. Regional
 864 ocean data assimilation. Annual Review of Marine Science 7, 21–42.
- 865 Emerick, A.A., Reynolds, A.C., 2013. Ensemble smoother with multiple data
 866 assimilation. Computers & Geosciences 55, 3 – 15. Ensemble Kalman filter
 867 for data assimilation.
- 868 Evensen, G., 1994. Sequential data assimilation with a nonlinear quasi-
 869 geostrophic model using monte carlo methods to forecast error statistics.
 870 Journal of Geophysical Research: Oceans 99, 10143–10162.
- 871 Evensen, G., van Leeuwen, P.J., 2000. An Ensemble Kalman Smoother for
 872 Nonlinear Dynamics. Monthly Weather Review 128, 1852–1867.
- 873 Farrell, B.F., Ioannou, P.J., 2001. State estimation using a reduced-order
 874 kalman filter. Journal of the Atmospheric Sciences 58, 3666–3680.
- 875 Heemink, A., Mouthaan, E., Roest, M., Vollebregt, E., Robaczewska, K.,
 876 Verlaan, M., 2002. Inverse 3d shallow water flow modelling of the conti-
 877 nental shelf. Continental Shelf Research 22, 465 – 484.
- 878 Jolliffe, I., Cadima, J., 2016. Principal component analysis: A review and
 879 recent developments. Philosophical Transactions of the Royal Society A:
 880 Mathematical, Physical and Engineering Sciences 374, 20150202.

- 881 Jongman, B., Ward, P.J., Aerts, J.C., 2012. Global exposure to river and
 882 coastal flooding: Long term trends and changes. *Global Environmental
 883 Change* 22, 823 – 835.
- 884 Karri, R.R., Badwe, A., Wang, X., El Serafy, G., Sumihar, J., Babovic, V.,
 885 Gerritsen, H., 2013. Application of data assimilation for improving forecast
 886 of water levels and residual currents in Singapore regional waters. *Ocean
 887 Dynamics* 63, 43–61.
- 888 Kernkamp, H., Van Dam, A., Stelling, G., de Goede, E., 2011. Efficient
 889 scheme for the shallow water equations on unstructured grids with appli-
 890 cation to the Continental Shelf. *Ocean Dynamics* , 1–14.
- 891 Kopp, G.A., FerreÂ', J.A., Giralt, F., 1997. The Use of Pattern Recog-
 892 nition and Proper Orthogonal Decomposition in Identifying the Structure
 893 of Fully-Developed Free Turbulence. *Journal of Fluids Engineering* 119,
 894 289–296.
- 895 Kosambi, D.D., 1943. Statistics in function space. *Journal of the Indian
 896 Mathematical Society* 7, 76–88.
- 897 Liang, Y.C., Lee, H.P., Lim, S.P., Lin, W.Z., Lee, K.H., Wu,
 898 C.G., 2002. Proper Orthogonal Decomposition and its APPLICA-
 899 TIONS—PART i: Theory. *Journal of Sound Vibration* 252, 527–544.
 900 doi:10.1006/jsvi.2001.4041.
- 901 Lin, B., McLaughlin, D., 2014. Efficient characterization of uncertain model
 902 parameters with a reduced-order ensemble kalman filter. *SIAM Journal on
 903 Scientific Computing* 36, B198–B224.
- 904 Lumley, J.L., 1967. The structure of inhomogeneous turbulence. *Atmospheric
 905 turbulence and radio propagation* , 166–178.
- 906 Lyard, F.H., Allain, D.J., Cancet, M., Carrère, L., Picot, N., 2021. Fes2014
 907 global ocean tide atlas: design and performance. *Ocean Science* 17,
 908 615–649. URL: <https://os.copernicus.org/articles/17/615/2021/>,
 909 doi:10.5194/os-17-615-2021.
- 910 Mahfouf, J.F., Rabier, F., 2000. The ecmwf operational implementation
 911 of four-dimensional variational assimilation. ii: Experimental results with

- 912 improved physics. Quarterly Journal of the Royal Meteorological Society
 913 126, 1171–1190.
- 914 Maraldi, C., Lyard, F., Testut, L., Coleman, R., 2011. Energetics of internal
 915 tides around the kerguelen plateau from modeling and altimetry. Journal
 916 of Geophysical Research: Oceans 116.
- 917 Mayo, T., Butler, T., Dawson, C.N., Hoteit, I., 2014. Data assimilation
 918 within the advanced circulation (adcirc) modeling framework for the esti-
 919 mation of manning's friction coefficient. Ocean Modelling .
- 920 Monahan, A.H., Fyfe, J.C., Ambaum, M.H.P., Stephenson, D.B., North,
 921 G.R., 2009. Empirical orthogonal functions: The medium is the message.
 922 Journal of Climate 22, 6501–6514.
- 923 Muis, S., Verlaan, M., Nicholls, R.J., Brown, S., Hinkel, J., Lincke, D., Vafei-
 924 dis, A.T., Scussolini, P., Winsemius, H.C., Ward, P.J., 2017. A comparison
 925 of two global datasets of extreme sea levels and resulting flood exposure.
 926 Earth's Future 5, 379–392.
- 927 Ngodock, H.E., Souopgui, I., Wallcraft, A.J., Richman, J.G.,
 928 Shriver, J.F., Arbic, B.K., 2016. On improving the accuracy
 929 of the m2 barotropic tides embedded in a high-resolution global
 930 ocean circulation model. Ocean Modelling 97, 16–26. URL:
 931 <https://www.sciencedirect.com/science/article/pii/S1463500315002140>,
 932 doi:<https://doi.org/10.1016/j.ocemod.2015.10.011>.
- 933 Pringle, W.J., Wirasaet, D., Roberts, K.J., Westerink, J.J., 2021.
 934 Global storm tide modeling with adcirc v55: unstructured mesh de-
 935 sign and performance. Geoscientific Model Development 14, 1125–
 936 1145. URL: <https://gmd.copernicus.org/articles/14/1125/2021/>,
 937 doi:10.5194/gmd-14-1125-2021.
- 938 Pugh, D., 1996. Tides, surges and mean sea-level. John Wiley & Sons, Ltd.
- 939 Pugh, D., Woodworth, P., 2014. Sea-Level Science: Understanding Tides,
 940 Surges, Tsunamis and Mean Sea-Level Changes. Cambridge University
 941 Press.
- 942 Ralston, M.L., Jennrich, R.I., 1978. Dud, A Derivative-Free Algorithm for
 943 Nonlinear Least Squares. Technometrics 20, 7–14.

- 944 Stammer, D., Ray, R.D., Andersen, O.B., Arbic, B.K., Bosch, W., Carrère,
 945 L., Cheng, Y., Chinn, D.S., Dushaw, B.D., Egbert, G.D., Erofeeva, S.Y.,
 946 Fok, H.S., Green, J.A.M., Griffiths, S., King, M.A., Lapin, V., Lemoine,
 947 F.G., Luthcke, S.B., Lyard, F., Morison, J., Müller, M., Padman, L., Rich-
 948 man, J.G., Shriver, J.F., Shum, C.K., Taguchi, E., Yi, Y., 2014. Accuracy
 949 assessment of global barotropic ocean tide models. *Reviews of Geophysics*
 950 52, 243–282.
- 951 Tozer, B., Sandwell, D.T., Smith, W.H.F., Olson, C., Beale, J.R., Wessel, P.,
 952 2019. Global bathymetry and topography at 15 arc sec: Srtm15+. *Earth*
 953 and Space Science
- 954 Trémolet, Y., 2007. Incremental 4d-var convergence study. *Tellus A* 59,
 955 706–718.
- 956 Verlaan, M., De Kleermaeker, S., Buckman, L., 2015. GLOSSIS: Global
 957 storm surge forecasting and information system [online]. Australasian
 958 Coasts & Ports Conference 2015: 22nd Australasian Coastal and Ocean
 959 Engineering Conference and the 15th Australasian Port and Harbour Con-
 960 ference. , 229–234.
- 961 Wang, X., Verlaan, M., Apecechea, M.I., Lin, H.X., 2021. Computation-
 962 efficient parameter estimation for a high-resolution global tide and surge
 963 model. *Journal of Geophysical Research: Oceans* 126, e2020JC016917.
- 964 Ward, P., Jongman, B., Salamon, P., Simpson, A., Bates, P., de Goeve,
 965 T., Muis, S., Coughlan, E., Rudari, R., Trigg, M., Winsemius, H., 2015.
 966 Usefulness and limitations of global flood risk models. *Nature Climate
 967 Change* 5, 712–715. doi:10.1038/nclimate2742.
- 968 Weatherall, P., Marks, K.M., Jakobsson, M., Schmitt, T., Tani, S., Arndt,
 969 J.E., Rovere, M., Chayes, D., Ferrini, V., Wigley, R., 2015. A new digital
 970 bathymetric model of the world's oceans. *Earth and Space Science* 2,
 971 331–345.
- 972 Zaron, E.D., 2019. Simultaneous estimation of ocean tides and underwater
 973 topography in the weddell sea. *Journal of Geophysical Research: Oceans*
 974 124, 3125–3148.

- ⁹⁷⁵ Zijl, F., Verlaan, M., Gerritsen, H., 2013. Improved water-level forecasting
⁹⁷⁶ for the northwest european shelf and north sea through direct modelling
⁹⁷⁷ of tide, surge and non-linear interaction. Ocean Dynamics 63, 823–847.

Highlights

Model order reduction significantly reduces the parameter estimation memory usage.

Estimation accuracy loss by the application of model order reduction is negligible.

Lengthening estimation time-span from 14 to 31 days improves the model performance.

Introducing outer iterations can improve the estimation effect for non-linear models.

Estimation of the bathymetry results in a significantly better accuracy for GTSM.

Author statement

Xiaohui Wang: Conceptualization, Methodology, Software, Writing – original draft.

Martin Verlaan: Conceptualization, Writing – review & editing, Supervision

Maialen Irazoqui Apecechea: Software

Hai Xiang Lin: Writing – review & editing, Supervision

Declaration of interests

The authors declare that they have no known competing financial interests or personal relationships that could have appeared to influence the work reported in this paper.

The authors declare the following financial interests/personal relationships which may be considered as potential competing interests: